An improved immersed boundary method with local flow pattern reconstruction and its validation ⊘

Wang Yudong (王煜栋) ⓘ ; Wang Fang (王方) ⓘ ; Zhou Jiawei (周佳伟) ⓘ ; Jin Jie (金捷) ✉ ⓘ

[Check for updates]

This study introduces an immersed boundary (IB) method based on coefficient array transformations of discrete equations for local cells and local flow pattern reconstruction, for the simulation of turbulent flow and combustion chemistry inside combustors with complex structure. This IB method is combined with a geometric scanning algorithm that traverses each fluid grid point in the vicinity of the wall, and based on the exact wall positions and normal vectors obtained from the scanning, the coefficient matrices of the individual grid points and their discrete forms of the governing equations are transformed, and the boundary conditions are added implicitly and exactly. The effectiveness of the method is validated through simulations of a cylinder, a gas turbine model combustor [Meier *et al.*, "Spray and flame structure of a generic injector at aeroengine conditions," in *Proceedings of the ASME 2011 Turbo Expo: Power for Land, Sea, and Air* (American Society of Mechanical Engineers, 2011), pp. 61–72 and Freitag *et al.*, "Measurement of initial conditions of a kerosene spray from a generic aeroengine injector at elevated pressure," Atomization Sprays **21**, 521 (2011)], and a specific aero-engine combustor, demonstrating precision comparable to traditional body-fitted mesh approaches, especially for complex combustor structures. The simulation demonstrates that the IB method achieves accuracy comparable to a fitted grid when it provides boundary information of similar quality and detail for control equations. The locally reconstructed IB method introduced in this paper successfully delivers high-precision boundary conditions, making it valuable for practical engineering applications.

I. INTRODUCTION

High-fidelity geometric reproduction is crucial for accurate numerical simulations. The IB method, pivotal in this context, captures the boundary's impact on flow fields by integrating source terms into discrete equations, as noted by Mittal and Iaccarino.[3] This approach enables complex geometry simulations without the challenges of body-fitted meshes, significantly easing the mesh generation workload.[4] Originally proposed by Peskin,[5] the IB method is widely applied in various fields, including flows near complex boundaries,[6–8] heat and mass transfer,[9,10] multi-phase flows,[11–13] and fluid–structure interactions,[14–16] serving as a vital link between fundamental research and engineering applications.

Recent years have seen significant efforts in advancing IB methods for accurately simulating high Reynolds number flows around complex geometries. This surge in research, initially inspired by Mohd-Yusof's discrete force method,[17] has led to the development of several high-accuracy IB methods suitable for simulating external flows with high Reynolds numbers. These methods primarily function by transferring boundary information to specific grid nodes. One notable example is the ghost cell method,[18] in which ghost cells are designated around the computational domain. At each ghost cell's center point M, orthogonal projection points on the physical boundary P are identified along with their normal vectors n. The physical domain's image points BI are defined symmetrically and assigned values using linear, bilinear, or quadratic reconstructions based on neighboring points. The Dirichlet or Neumann conditions are then translated into an equivalent Dirichlet condition at the center point M of the ghost cell via a simple extrapolation of the BI and P values. Further sophistication is seen in a second-order approximation with Neumann conditions, achievable through an expansion along several points on the half-line (M, n).[19–21] In parallel with these developments, reconstruction-based schemes have also garnered significant attention. Pioneered by researchers such as Ye *et al.*,[22] Majumdar *et al.*,[23] Udaykumar *et al.*,[24] and Lee,[25] these schemes focus on reconstructing the flow field near the boundaries by interpolating data from the fluid domain. Their approach typically involves higher-order polynomial reconstructions, offering a potent alternative to traditional methods, especially in dealing

with complex geometries and boundary conditions. These schemes have been proven to be effective in improving accuracy and stability in high Reynolds number flow simulations. Additionally, Shu *et al.*[26,27] innovated by using the governing equations to extrapolate the derivative values of numerical solutions to the boundary points, specifying the inflow conditions, and approximating the phantom values through Taylor expansions. For outflow boundaries, they employed an extrapolation technique based on the weighted essentially non-oscillatory (WENO) method. This method achieves higher-order accuracy when data are smoothed, and recently proposals for fourth-/fifth-order reconstructions along the normal have been put forward. However, these techniques have limitations; they are problem-dependent,[28,29] require varying treatments for different boundary types, and are relatively computationally demanding. Addressing these issues, Clain *et al.*[30] introduced an off-site data reconstruction method, developing an IB method that attains at least sixth-order accuracy in smooth domains. Furthermore, Appelo and Petersson[31] proposed using internal boundary points to eliminate the small cell stiffness problem for Dirichlet and Neumann conditions, offering a robust solution compared to previous methods reliant on external ghost points and achieving up to fourth-order accuracy.

In numerical simulations of turbulent combustion, the accuracy at grid boundaries is contingent on how closely the employed boundary conditions resemble the true physical boundaries. IB methods on non-fitted grids exhibit less overlap with actual boundaries compared to boundary-fitted grid algorithms, often resulting in lower accuracy at computational domain edges. To enhance simulation precision, local grid refinement near boundaries is frequently employed in conjunction with the IB method.[32–34] This approach aims to align the fluid region's boundary more closely with the real wall, thereby improving the fidelity of the modeled boundary conditions. Additionally, supplementing control equations at points near the boundary-fitted grid with information from the actual wall can further increase flow field simulation accuracy in IB method-based studies.

The IB method, commonly employed with cartesian grids, distinguishes solid and fluid domains through grid point labeling, essential for internal flow simulations in complex geometries. Traditional applications without local refinement or domain-shape optimization can lead to computational inefficiency. Various efforts to address this issue, including Anupindi *et al.*'s[35] small-volume chunking approach, Delorme *et al.*'s[36] grid utilization tests, de Zelicourt *et al.*'s[37] fluid grid reindexing, and Zhu *et al.*'s[38] parallelization with open-source software, have met with mixed success. This paper proposes an IB method that utilizes a curvilinear coordinate system grid closely aligned with the fluid domain shape, significantly improving computational efficiency, especially in thin-walled structures like gas turbine combustors.

Real aero-engine combustors, with their complex structures, challenge high-quality mesh generation. Body-fitted mesh topologies, common in basic research, lack the flexibility needed for these combustors.[39] While commercial software often utilizes unstructured grids,[40] these can be inefficient for high-fidelity turbulent combustion simulations due to long addressing times, convergence difficulties, and complex parallelization. However, the IB method offers a reduction in meshing workload while retaining structural mesh topology, suitable for aero-engine combustor simulations. Despite its lower spatial accuracy,[41] the IB method's demand for high-density boundary meshes[42] aligns well with the large eddy simulation (LES) and transported probability density function (TPDF) turbulent combustion model's requirements.[43,44] This paper introduces an IB method tailored for gas turbine combustors, integrating local flow pattern reconstruction and a geometric structure scanning algorithm, combined with the LES-TPDF model.[45,46] The validation of the IB method begins with cylinder flow at Reynolds number 3900 and a dual-stage swirler model combustor, subsequently extending to a real aircraft engine combustor to demonstrate its engineering applicability and bridging the gap between basic research and practical engineering.

II. METHODOLOGY

### A. Grid labels generation and wall information resolution

In this method, the flow field and embedded solids are treated as a cohesive system. The method models the impact of the solid boundary on the flow through the source terms in the governing equations, and vice versa, by interpolating the fluid's velocity at the boundary.[47] For simulating turbulent combustion in complex-geometry combustors, this method requires mapping the combustor geometry onto a background mesh using

grid labels, differentiating fluid and solid domains. After this mapping, source terms are integrated into control equations post coordinate transformation and discretization, facilitating application in curvilinear coordinates.

In this study, we utilize the Möller–Trumbore algorithm, a staple in ray tracing,[48] for generating grid labels integral to simulating turbulent two-phase combustion using the IB method. This involves scanning the stereolithography (STL) format geometrical model aligned with the computational domain's grid coordinates. Grid labels are determined on the basis of the count of line intersections with the model, providing a foundational step for applying the IB method in numerical simulations.

Any point on the scanning line can be denoted as $P = O + \alpha D$, where O is the starting point, D is the scanning direction, and α is any real number. If a point in the background grid can be represented as $O + \alpha D$, the scan line has two intersections with the geometry, $O + \alpha_1 D$ and $O + \alpha_2 D$, and if $\alpha_1 < \alpha_0 < \alpha_2$ or $\alpha_2 < \alpha_0 < \alpha_1$, then the grid point lies inside the geometry, otherwise the point lies outside the geometry as shown in **Fig. 1**, and grid points are labeled accordingly as fluid or solid.

FIG. 1.
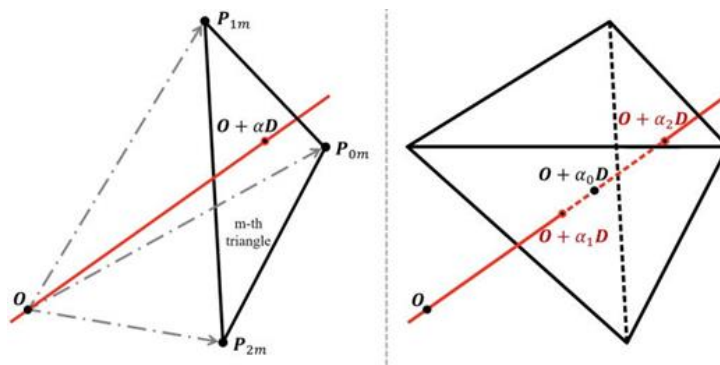
Schematic diagram of the scanning algorithm.

To improve efficiency, if a linear coordinate axis exists in the coordinate system corresponding to the background mesh, a scanning line is generated by grouping points parallel to this coordinate axis and in the other two directions as scanning points. The set of triangular faces in the geometric model that may have intersections with this scanning line is selected according to the coordinate range, and the three vertices of the mth triangular face in this set are denoted as P_{0m}, P_{1m}, and P_{2m}, and satisfy the following equation:

$$O + \alpha D = (1 - b_1 - b_2)P_{0m} + b_1 P_{1m} + b_2 P_{2m},$$

◀ ▬▬▬▬▬▬▬▬ ▶

(1)

◀ ▬▬▬▬▬▬▬▬ ▶　　　　　where b_1 and b_2 are arbitrary real numbers, and α in

$$\alpha = \frac{E_2 \cdot S_2}{E_1 \cdot S_1},$$

(2)

◀ ● ▶

Eq. **(1)** can be determined using Cramer's rule and can be expressed as　　　　where $E_1 = P_{1m} - P_{0m}$, $E_2 = P_{2m} - P_{0m}$, $S_1 = D \times E_2$, $S_2 = S \times E_1$, and $S = O - P_{0m}$.

$$b_1 = \frac{S \cdot S_1}{E_1 \cdot S_1}, \quad b_2 = \frac{D \cdot S_2}{E_1 \cdot S_1}.$$

(3)　　　　　(4)

◀ ● ▶　◀ ● ▶

Similarly, it can be inferred that

After that, it is judged whether the three conditions $b_1 \geq 0$, $b_2 \geq 0$, $b_1 + b_2 \geq 0$ are satisfied. If they are satisfied, then there exists an intersection point (noted as point m) between the scan line and the current triangular plane, and the position of the intersection point is $P = O + \alpha D$.

Upon iterating through the complete set of triangulated surfaces that may intersect with this scan line, all grid points on the scan line are identified and classified as either fluid or solid points based on the intersection set. Specifically, when the model entity is a solid domain, the grid points located after the intersection point with

an odd number to before the intersection point with an even number are labeled as solid nodes, and the others are labeled as fluid nodes.

B. IB method with local flow pattern reconstruction

In the conventional IB method, the body force term is generally solved explicitly, and thus there is no guarantee that the fluid velocity along the structural boundary is equal to the solid wall velocity, which means that the no-slip boundary condition may not be satisfied at the solid wall.[47,49] The implicit IB method in this study is applied to simulation of flow inside a complex structure exemplified by a combustor, and it is considered that the wall is rigid and stationary constant, and there is no numerical rigidity of the IB method caused by the difference between the large coefficients of elasticity of the wall and small viscosities of the fluid,[50,51] and that the no-slip of the sharp interface form can be realized implicitly by dealing with the array of coefficients of the discrete equations in the vicinity of the wall and the Neumann boundary conditions.

In combustor simulations using the IB method, the key goal is to accurately translate real wall boundary conditions into source terms in the control equation system. However, the grids near the wall (P) often differ from the actual wall shape, as depicted in **Fig. 2**, leading to discrepancies in the solid domain shape and loss of critical information like the wall's position and normal vector. This misalignment can result in imprecise boundary condition representation in the source terms derived from grid labels.

FIG. 2.
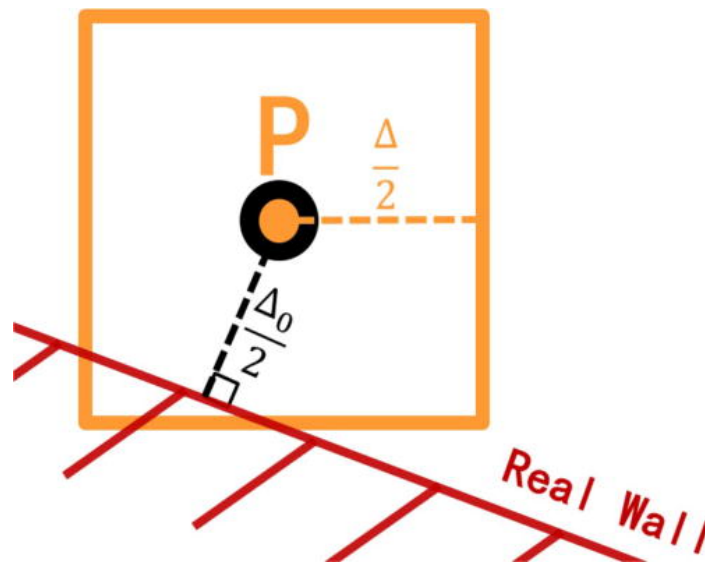
Schematic of the fluid grid near the wall.

In contrast, when body-fitted mesh is employed, the grid edges near the wall surface align more closely with the actual wall contours. This alignment results in boundary conditions that more accurately represent the wall's position and normal vectors, thereby enhancing simulation precision near boundaries.

In a specific scenario, contemplate a situation where the edges of a grid denoted as P closely align with the actual wall in the application of the IB method, and the neighboring grid, denoted as S, is designated as the solid domain, as depicted in **Fig. 3**. In this case, the grid P encapsulates information regarding the position of the wall and normal vectors that align with the precision expected in a body-fitted mesh of the same scale, thereby enabling simulation accuracy comparable to the performance achieved by algorithm under the body-fitted mesh.

FIG. 3.
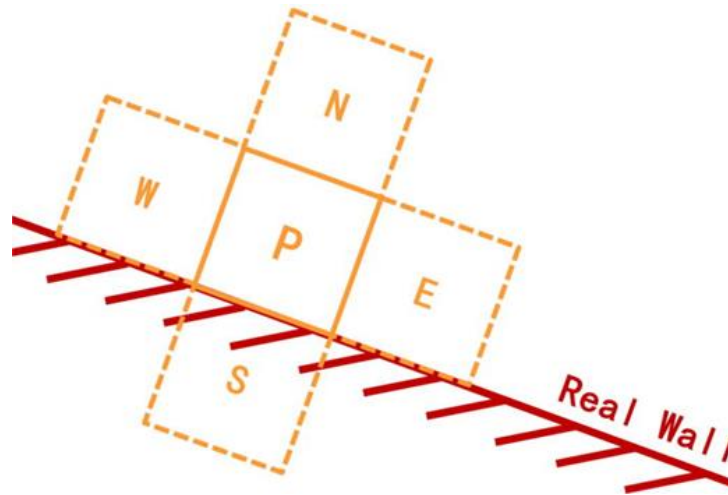
Schematic diagram of body-fitted mesh near the wall.

For the general case where the IB method is applied, the edges of the grid close to the wall may not coincide with the real wall, that is, the width of the grid P closest to the wall is Δ, the grid on its southern side is S, and the face between the two grids is s, but the actual distance between the center of this grid and the wall $\frac{\Delta_0}{2}$, Obviously, Δ_0 satisfies $0 < \frac{\Delta_0}{2} < \Delta$. In the finite-volume method commonly employed in combustor simulations, variable values within the control volume are typically treated as volume averages and stored at the center of the grids.

Three assumptions are postulated concerning the fluid grid in close proximity to the walls. First, it is assumed that a negligible alteration in the grid scale (less than $\frac{\Delta}{2}$) does not result in a modification of the scalar value associated with the grid after volume averaging (or box filtering in large-eddy simulation), giving the equation:

$$\widetilde{\phi_P} = \widetilde{\phi_{P_0}},$$

(5)

◀ ● ▶   where $\widetilde{\phi_P}$ denotes the value of the variable stored in the original grid P after volume averaging, and $\widetilde{\phi_{P_0}}$ denotes the value of the variable in the new grid P_0 obtained after the change of grid scale.

The second assumption posits that the scalar exhibits a linear distribution between grid P and its adjacent grids. Following the adjustment of the scale of grid P as per the initial assumption, the scales of the neighboring grids undergo a proportional change. The grids necessary for solving the system of discrete equations at this location after the transform from P, N, S, W, E, L, R to P_0, N_0, S_0, W_0, E_0, L_0, R_0, as illustrated in **Fig. 4**.

FIG. 4.
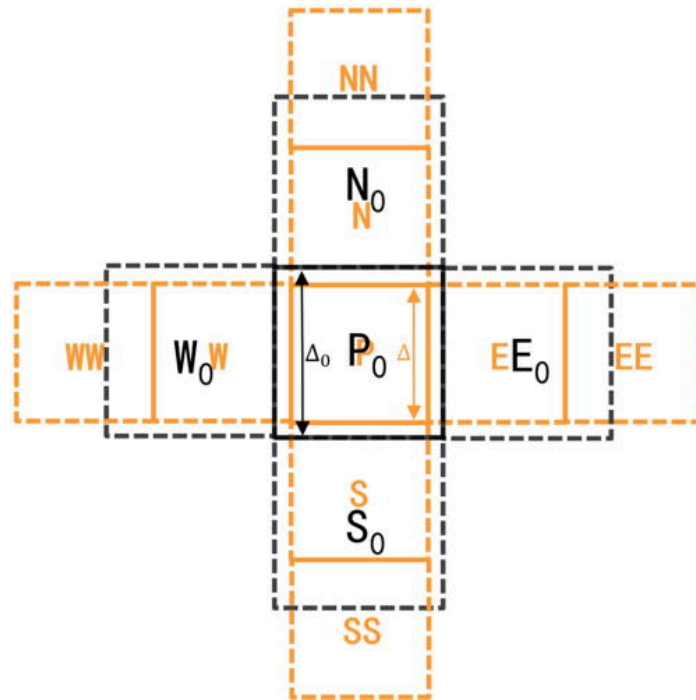
Schematic diagram of grid scale transformation.

According to the second assumption, the scalar values in the grids adjacent to P_0 after the transformation

$$\widetilde{\phi_{N_0}} = \frac{\Delta - \Delta_0}{\Delta + \Delta_N} \widetilde{\phi_P} + \frac{\Delta_N + \Delta_0}{\Delta + \Delta_N} \widetilde{\phi_N}.$$

(6)

can be obtained through interpolation. Taking $\widetilde{\phi_{N_0}}$ as an example,

The third assumption is that the scalar is linearly distributed over any arc of the sphere with the center of the grid P_0 as the center and $\frac{\Delta_0}{2}$ as the radius. The arc-shaped interpolation assumption in finite volume methods is rationalized by the isotropic scalar distributions in fluids at small scales, allowing a uniform approximation within a spherical control volume and avoiding the computational cost of higher order reconstruction. The case of two-dimensional rotation is first discussed, such that the axis of rotation is parallel to the coordinate axis ζ_3. Under the third assumption, one can interpolate to find the value of the scalar at any point on a circle centered at the center of P_0 and of radius $\frac{\Delta_0}{2}$. For example, for the point N_3 in **Fig. 5**, the

$$\widetilde{\phi_{N_3}} = \frac{2\theta}{\pi} \widetilde{\phi_{E_0}} + \frac{\pi - 2\theta}{\pi} \widetilde{\phi_{N_0}}.$$

(7)

scalar value of the point can be found by interpolation based on Eq. **(7)**.
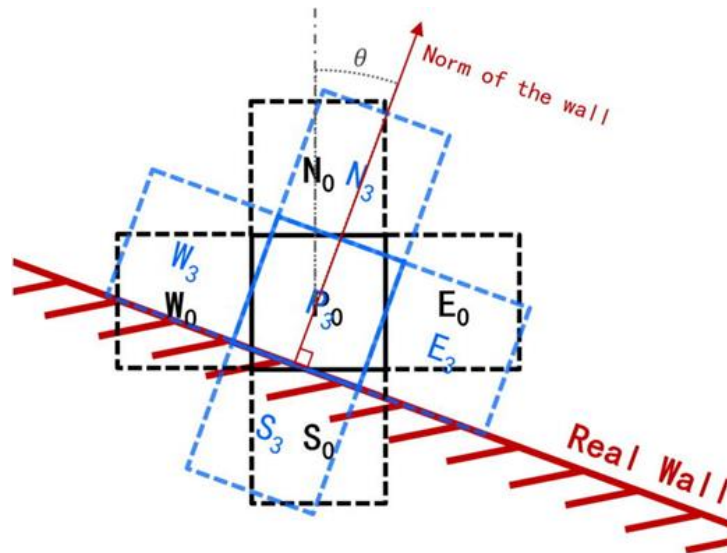
FIG. 5.
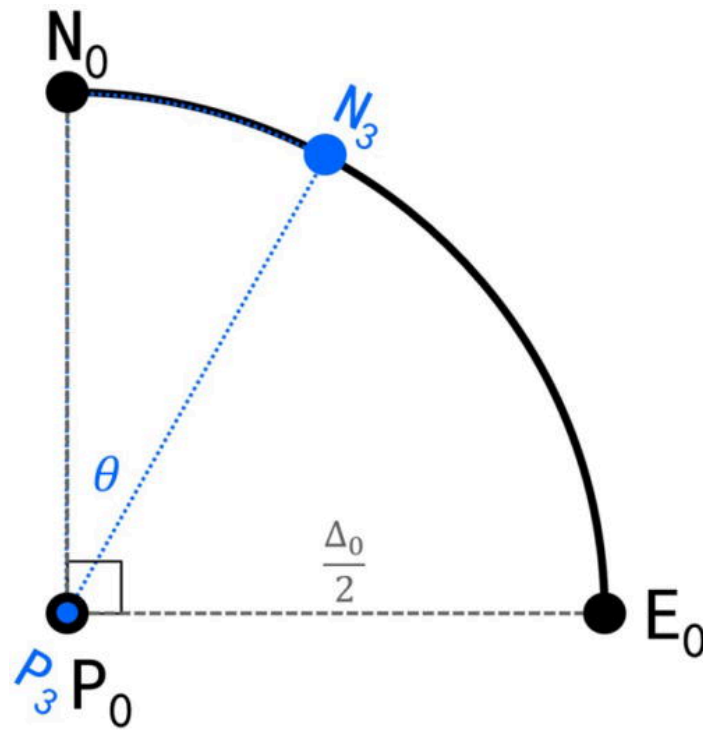
Schematic of the interpolation points on the circle.

From the above equation, the scale transformed grid can be rotated at an angle θ, and it is obvious that $0 < \theta < \frac{\pi}{2}$, after the change, the grid corresponding to solving the system of discrete equations at this position changes from P_0, N_0, S_0, W_0, E_0, L_0, R_0 to P_3, N_3, S_3, W_3, E_3, L_3, R_3 as shown in **Fig. 6**.

FIG. 6.

Schematic of grid rotation transformation.

Make $\Sigma A_{\text{side}}\widetilde{\phi_{\text{side}}} = A_{\text{N}}\widetilde{\phi_{\text{N}}} + A_{\text{S}}\widetilde{\phi_{\text{S}}} + A_{\text{W}}\widetilde{\phi_{\text{W}}} + A_{\text{E}}\widetilde{\phi_{\text{E}}} + A_{\text{L}}\widetilde{\phi_{\text{L}}} + A_{\text{R}}\widetilde{\phi_{\text{R}}}$ and
$\Sigma A_{\text{side}_0}\widetilde{\phi_{\text{side}_0}} = A_{\text{N}_0}\widetilde{\phi_{\text{N}_0}} + A_{\text{S}_0}\widetilde{\phi_{\text{S}_0}} + A_{\text{W}_0}\widetilde{\phi_{\text{W}_0}} + A_{\text{E}_0}\widetilde{\phi_{\text{E}_0}} + A_{\text{L}_0}\widetilde{\phi_{\text{L}_0}} + A_{\text{R}_0}\widetilde{\phi_{\text{R}_0}}$ and so on. In the

generalized form of the discrete equations, for the original grid P and the transformed grid P_3, respectively,

$$A_P \widetilde{\phi_P} = \Sigma A_{\text{side}} \widetilde{\phi_{\text{side}}} + S, \quad A_{P_3} \widetilde{\phi_{P_3}} = \Sigma A_{\text{side}_3} \widetilde{\phi_{\text{side}_3}} + S_3.$$

(8)   (9)

Considering the box-filtered scalar $\widetilde{\phi}$ in the finite-volume method as a volume average, the source term S is considered to be unchanged before and after the transformation, i.e., $S_1 = S_0 = S$, so that there are

$$\Sigma A_{\text{side}} \widetilde{\phi_{\text{side}}} - A_P \widetilde{\phi_P} = \Sigma A_{\text{side}_0} \widetilde{\phi_{\text{side}_0}} - A_{P_0} \widetilde{\phi_{P_0}} = \Sigma A_{\text{side}_3} \widetilde{\phi_{\text{side}_3}} - A_{P_3} \widetilde{\phi_{P_3}}.$$

(10)

$$\widetilde{\phi_{S_0}} = k_0 \widetilde{\phi_S} + (1 - k_0) \widetilde{\phi_P}.$$

(11)

Under the second assumption, let denote $k_0 = \frac{\Delta_0 + \Delta_S}{\Delta + \Delta_S}$, then

Substituting Eq. (11) into Eq. (10) and simplifying give

$$\Sigma A_{\text{side}} \widetilde{\phi_{\text{side}}} - A_P \widetilde{\phi_P} = \Sigma k_0 A_{\text{side}_0} \widetilde{\phi_{\text{side}}} - ((1 - k_0) \Sigma A_{\text{side}_0} + A_{P_0}) \widetilde{\phi_P}.$$

(12)

The correspondence of the coefficient array before and after the volume transformation is obtained by actual backpropagation in Eq. (12). $\widetilde{\phi_N}$, $\widetilde{\phi_S}$, $\widetilde{\phi_W}$, $\widetilde{\phi_E}$, $\widetilde{\phi_L}$, $\widetilde{\phi_R}$ are unknown scalars that lie on both sides of the equation at the same time, and there exist infinite kinds of value, so there are

$$
\begin{bmatrix}
A_N \\
A_S \\
A_W \\
A_E \\
A_L \\
A_R \\
A_P
\end{bmatrix}
=
\begin{bmatrix}
k_0 A_{N_0} \\
k_0 A_{S_0} \\
k_0 A_{W_0} \\
k_0 A_{E_0} \\
k_0 A_{L_0} \\
k_0 A_{R_0} \\
(1 - k_0) \Sigma A_{side_0} + A_{P_0}
\end{bmatrix}.
$$

(13)

Similarly, for a rotational transformation around the ζ_3 axis, let $k_3 = \frac{\pi - 2\theta}{\pi}$, where $0 < \theta \leq \frac{\pi}{4}$, then

$$
\begin{bmatrix}
A_{N_0} \\
A_{S_0} \\
A_{W_0} \\
A_{E_0} \\
A_{L_0} \\
A_{R_0} \\
A_{P_0}
\end{bmatrix}
=
\begin{bmatrix}
k_3 A_{N_3} + (1 - k_3) A_{W_3} \\
k_3 A_{S_3} + (1 - k_3) A_{E_3} \\
k_3 A_{W_3} + (1 - k_3) A_{S_3} \\
k_3 A_{E_3} + (1 - k_3) A_{N_3} \\
A_{L_3} \\
A_{R_3} \\
A_{P_3}
\end{bmatrix}.
$$

(14)

Equation (14) is the coefficient array correspondence before and after the grid P and its neighboring grids rotate $\frac{(1-k_3)\pi}{2}$ clockwise around the ζ_3 axis. For the three-dimensional case, in order to rotate one side of the grid to coincide with the real wall, it may be necessary to rotate it about the ζ_2 and ζ_1 axes in addition to the rotation about the ζ_3 axis. Assuming that the angles of clockwise rotation around the ζ_2 and ζ_1 axes are the $\frac{(1-k_2)\pi}{2}$ and $\frac{(1-k_1)\pi}{2}$, respectively, the coefficient-array correspondences for the three-dimensional rotations

$$\begin{bmatrix} A_{N_3} \\ A_{S_3} \\ A_{W_3} \\ A_{E_3} \\ A_{L_3} \\ A_{R_3} \\ A_{P_3} \end{bmatrix} = \begin{bmatrix} k_2 A_{N_2} + (1-k_2)A_{R_2} \\ k_2 A_{S_2} + (1-k_2)A_{L_2} \\ A_{W_2} \\ A_{E_2} \\ k_2 A_{L_2} + (1-k_2)A_{N_2} \\ k_2 A_{R_2} + (1-k_2)A_{S_2} \\ A_{P_2} \end{bmatrix},$$

(15)

can be generalized based on the rotations discussed above,

$$\begin{bmatrix} A_{N_2} \\ A_{S_2} \\ A_{W_2} \\ A_{E_2} \\ A_{L_2} \\ A_{R_2} \\ A_{P_2} \end{bmatrix} = \begin{bmatrix} A_{N_1} \\ A_{N_1} \\ k_1 A_{W_1} + (1-k_1)A_{R_1} \\ k_1 A_{E_1} + (1-k_1)A_{L_1} \\ k_1 A_{L_1} + (1-k_1)A_{W_1} \\ k_1 A_{R_1} + (1-k_1)A_{E_1} \\ A_{P_1} \end{bmatrix}.$$

(16)

After scale transformation and 3D rotation transformation, the relevant grid points at the current position are transformed from P, N, S, W, E, L, R to P_0, N_0, S_0, W_0, E_0, L_0, R_0, where one side of the grid coincides with the wall. P_1 can be treated as a boundary-fitted grid and process its coefficient array to implicitly add wall boundary conditions. As an example, the neighboring grid S_1 of P_1 is a solid wall, and for the momentum

$$S_{\text{mom}} = -A_{S_1}\widetilde{\phi_{S_1}} + S_{\text{wall}_1},$$

(17)

equation, a source term S_{mom} should be added: where S_{wall_1} denotes the source term for wall shear stress formation, which can be given by the wall function, and is derived from the wall information corresponding to P_1 obtained after the reconstruction.

Adding the source term - $A_{S_1}\tilde{\phi}_{S_1}$ to the discretization equation for this grid point enables the $\tilde{\phi}_{S_1}$ term in the discretization equation to be canceled out, which corresponds to a constant velocity of 0 for the grid S_1, thus realizing the no-slip boundary condition.

For the discrete equations corresponding to the transport equations for the scalar quantities of substance concentration and enthalpy in the LES-TPDF method,[43,44] add the source term S_{scalar}:

$$S_{\text{scalar}} = A_{S_1}(\widetilde{\phi_{P_1}} - \widetilde{\phi_{S_1}}).$$

(18)

For discrete equations at the point of the grid P_1, this is equivalent to making $\tilde{\phi}_{P_1}$ constantly equal to $\tilde{\phi}_{S_1}$, thus achieving the boundary condition of the zero gradient.

According to Eqs. (13)–(18), the discrete equations localized for P_1 with exact boundary conditions can be obtained. However, the discrete equations actually solved in the turbulent combustion simulation are specific to P and are solved for the computational domain as a whole. As shown in Eq. (10), considering that the source term represents the physical quantity after volume averaging in the finite volume method, there is $S_1 = S$. Therefore, the source term S_1 can be brought back to S directly to realize the inverse transformation from P_1 to P. After that, the IB method is realized based on the local reconstruction of the coefficient array.

C. LES-TPDF turbulent combustion model

The LES methodology uses a filtering function to resolve flow field variables above a designated scale. Subgrid-scale models are employed to represent the effects of smaller scales. This method is widely applied in engineering to explicitly capture the larger eddies that carry the bulk of turbulent energy. The TPDF model deals with turbulent combustion by fully closing the chemical reaction source terms without resorting to low-dimensional manifold assumptions. This results in enhanced accuracy, particularly when integrated with complex chemical kinetics. In this paper, we amalgamate the IB method, as referenced in Sec. II B, with the LES-TPDF approach to facilitate the simulation of turbulent combustion within combustors featuring intricate geometrical constructs. To reduce the number of grid points in solid regions resulting from the complex flow passages of the combustor, a coordinate transformation is used within a curvilinear framework. The Jacobian matrix, $J_{ij} = \frac{\partial x_i}{\partial \zeta_j}$, is essential for this transformation. The curvilinear coordinates of the background grid are represented by x_i, while ζ_j represents the Cartesian coordinates after transformation. This allows the chain rule to be applied to the filtered Navier–Stokes equations post-LES. The resulting mass conservation equation, energy conservation equation, and scalar (including enthalpy and species mass fraction) transport

$$\frac{\partial \overline{\rho}}{\partial t} + \frac{\partial}{\partial \zeta_k}\left(\frac{A_{ki}}{|\boldsymbol{J}|} \overline{\rho}\widetilde{u}_i \right) = 0,$$

(19)

equation are as follows:

$$\frac{\partial \overline{\rho}\widetilde{u}_i}{\partial t} + \frac{\partial}{\partial \zeta_k}\left(\frac{A_{kj}}{|\boldsymbol{J}|} \overline{\rho}\widetilde{u}_i\widetilde{u}_j \right) = -\frac{A_{ki}}{|\boldsymbol{J}|}\frac{\partial \overline{p}}{\partial \zeta_k} + \frac{\partial}{\partial \zeta_k}\left(\frac{A_{ki}}{|\boldsymbol{J}|}\left(\mu_{\mathrm{t}}\frac{A_{lj}}{|\boldsymbol{J}|}\frac{\partial \widetilde{u}_i}{\partial \zeta_l} + \mu_{\mathrm{t}}\frac{A_{li}}{|\boldsymbol{J}|}\frac{\partial \widetilde{u}_j}{\partial \zeta_l} \right) \right),$$

(20)

$$\frac{\partial \overline{\rho}\widetilde{\phi}}{\partial t} + \frac{\partial}{\partial \zeta_k}\left(\frac{A_{ki}}{|\boldsymbol{J}|} \overline{\rho}\widetilde{u}_i\widetilde{\phi} \right) = \frac{\partial}{\partial \zeta_k}\left(\frac{A_{ki}}{|\boldsymbol{J}|}\left(\mu_{\mathrm{t}}\frac{A_{li}}{|\boldsymbol{J}|}\frac{\partial \widetilde{\phi}}{\partial \zeta_l} \right) \right).$$

(21)

In the above equations, $\overline{\rho}$ represents the mean density; μ_{t} denotes the sum of molecular viscosity and subgrid-scale turbulent viscosity; $\widetilde{u}_i$ is the density-weighted filtered velocity component in the ith direction; t signifies the time; ϕ is a vector composed of scalars including species concentration and mixture enthalpy; and A corresponds to the area of a face on a hexahedral grid.

Building upon Eq. (21) and following the methodology outlined by Gao and O'Brien,[52] an evolution equation for the density-weighted sub-grid PDF can be deduced to describe the scalar quantities essential for chemical reactions. This PDF is governed by a transport equation, encapsulating both the advection by resolved scales and the effects of unresolved scales, where the latter demands modeling. For sub-grid scale transport, the Smagorinsky model is utilized, while the linear mean square estimation[53] is adopted for micro-mixing. These modeling choices empower the employment of TPDF methods, enhancing the accuracy of predictions for turbulent mixing and reaction rates in combustor simulations. The resulting TPDF equation[54] for the scalars is denoted as follows:

$$\overline{\rho}\frac{\partial \widetilde{P}_{\mathrm{sgs}}(\boldsymbol{\psi})}{\partial t} + \overline{\rho}\widetilde{u}_j\frac{\partial \widetilde{P}_{\mathrm{sgs}}(\boldsymbol{\psi})}{\partial x_j} + \sum_{\alpha=1}^{N_s}\frac{\partial}{\partial \psi_\alpha}\left[\overline{\rho}\omega_\alpha(\boldsymbol{\psi})\widetilde{P}_{\mathrm{sgs}}(\boldsymbol{\psi}) \right] = \frac{\partial}{\partial x_i}\left(\mu_{\mathrm{t}}\frac{\partial \widetilde{P}_{\mathrm{sgs}}(\boldsymbol{\psi})}{\partial x_i} \right) - \frac{C_{\mathrm{d}}}{\tau_{\mathrm{sgs}}}\sum_{\alpha=1}^{N_s}\frac{\partial}{\partial \psi_\alpha}\left(\overline{\rho}(\psi_\alpha - \phi_\alpha)\widetilde{P}_{\mathrm{sgs}}(\boldsymbol{\psi}) \right),$$

(22)

where $\widetilde{P}_{\mathrm{sgs}}(\boldsymbol{\psi})$ represents the sub-grid PDF of the scalar array ϕ; N_s denotes the total number of species, including enthalpy; $\dot{\omega}_\alpha$ is the reaction rate of species α; τ_{sgs} is the sub-grid mixing timescale;[55] and $C_{\mathrm{d}} = 2.0$.[56]

Equation (22) can be transformed by introducing the Eulerian stochastic field method proposed by Valiño and co-authors[57] as follows:

$$\overline{\rho}\frac{\partial \xi}{\partial t} = -\overline{\rho}\widetilde{u}_j\frac{\partial \xi}{\partial x_j} + \frac{\partial}{\partial x_j}\left(\Gamma\frac{\partial \xi}{\partial x_j} \right) + \overline{\rho}\sqrt{\frac{2\Gamma}{\overline{\rho}}}\frac{\partial \xi}{\partial x_j}\frac{\mathrm{d}W_j}{\Delta t} - 0.5C_{\mathrm{d}}\frac{\overline{\rho}}{\tau_{\mathrm{sgs}}}(\xi - \widetilde{\phi}) + \overline{\rho}\omega(\xi)$$

(23)

where ξ is the random variable in the random field, corresponding to the scalar ϕ; $\mathrm{d}W_j$ represents the Wiener process; and Γ represents the total diffusion coefficient.

Equations **(19)**, **(20)**, and **(23)** all take the form of transport equations, which can be integrated and discretized into the form presented by Eq. **(8)**. In this paper, the proposed IB method is integrated and applied within an internal software framework for turbulent flame simulation, which is based on body-fitted structured grids and the LES-TPDF approach. The spatial discretization is conducted using a second-order central difference scheme, while time discretization is achieved through the Crank–Nicolson scheme, ensuring accurate and efficient simulation of turbulent combustion phenomena. **Figure 7** below illustrates the general procedure for simulating a combustor using the LES-TPDF approach in conjunction with the IB method.

FIG. 7.
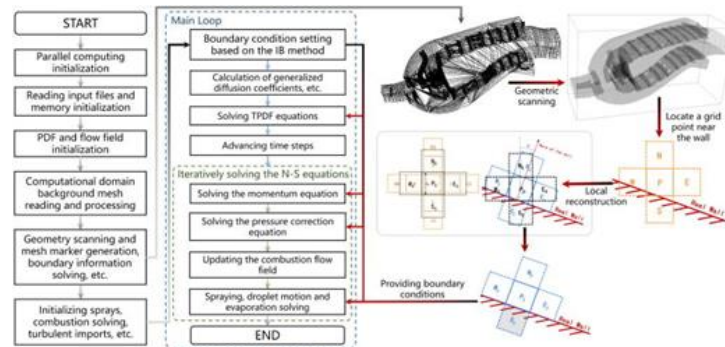
Schematic of combustion simulation based on IB method and LES-TPDF.

III. RESULTS AND DISCUSSION

A. Flow past a cylinder at Reynolds number 3900

The study of flow around a cylinder is a widely discussed topic in computational fluid dynamics (CFD), known for its simple geometry, yet encapsulating critical flow characteristics such as flow separation, vortex generation, and dissipation, common in turbulent flows. This phenomenon is prevalent in both everyday life and engineering applications. The IB method, reconstructed based on the flow manifold near boundaries, was applied to simulate cylinder flow at a Reynolds number of 3900. This research involved comparing the average flow field and flow pulsations obtained via this IB method with results from a body-fitted mesh approach and experimental data. The comparison aimed to evaluate the accuracy of the discrete equations for fluid domain boundaries employed in this IB method against the boundary conditions achieved with the body-fitted mesh approach.

In this case, the diameter of the cylinder is D = 0.02 m, with an inlet air velocity of $U_c = 2.896\,68$ m/s. This study employs a mesh size range of 0.2–0.8 mm and a total mesh count of 6.89×10^6, following the grid independence analysis detailed by Sarkar and Sarkar,[58] which demonstrated that mesh refinement beyond this level does not significantly affect key flow parameters such as drag coefficient and Strouhal number. Near the cylinder, the mesh is refined based on coordinate transformation, divided into 64 parallel blocks to ensure load balancing. **Figure 8** illustrates the background mesh used to simulate the flow around the cylinder.

FIG. 8.
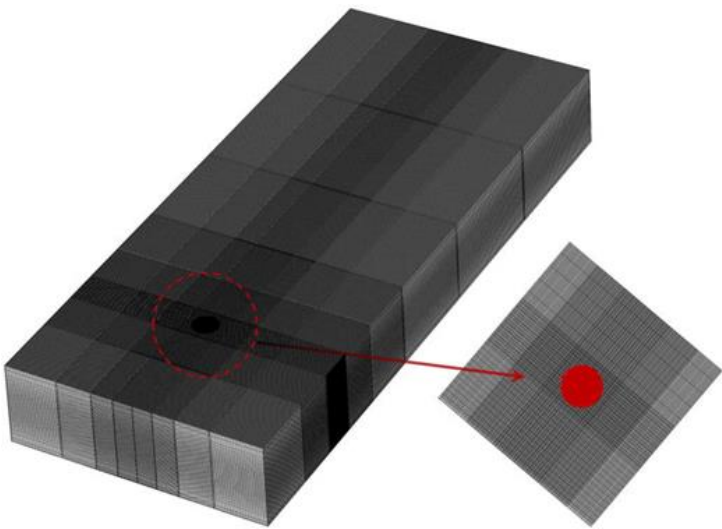
Mesh for simulating flow past a cylinder.

The simulation results, depicted in **Fig. 9** (Multimedia available online) and **Fig. 10**, reveal the relative velocity distribution around the cylinder. In particular, a recirculation zone, or a wake, forms behind the cylinder, with the lowest average flow velocity recorded at −0.8867 m/s. This minimum velocity point is centrally located on the Y–Z planes, at a distance of 0.0288 m from the center of the cylinder.
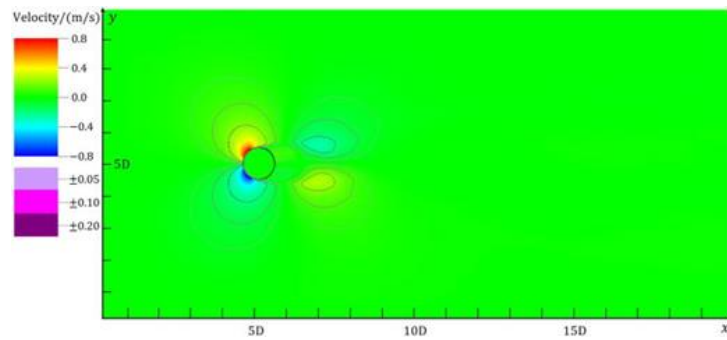
FIG. 9.
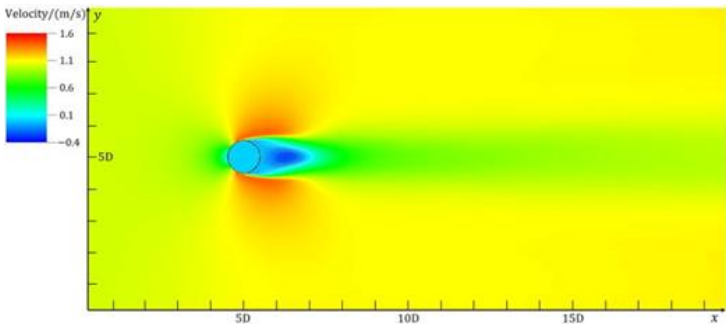
Time-averaged streamwise relative velocity distribution. Multimedia available online.
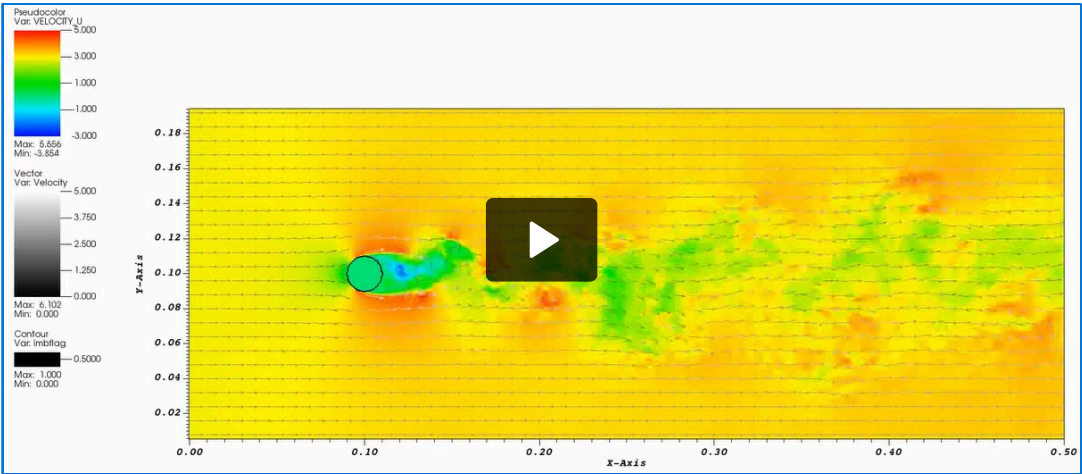
[Video/Audio] available online

FIG. 10.

Time-averaged transverse relative velocity distribution.

[Figure 11](#) presents the distribution of time-averaged relative velocities along the x axis at the central line, where x/D denotes the relative distance from the cylinder's center. The results of the IB method based on local reconstruction are compared with the simulation and experimental results of Parnaudeau *et al.*,[59] Ma *et al.*,[60] and Lourenco.[61] The simulated time-averaged velocity distribution closely aligns with Parnaudeau's particle image velocimetry (PIV) measurements, with the minimum velocity value and its location falling between the experimental data of Parnaudeau and Lourenco.

FIG. 11.
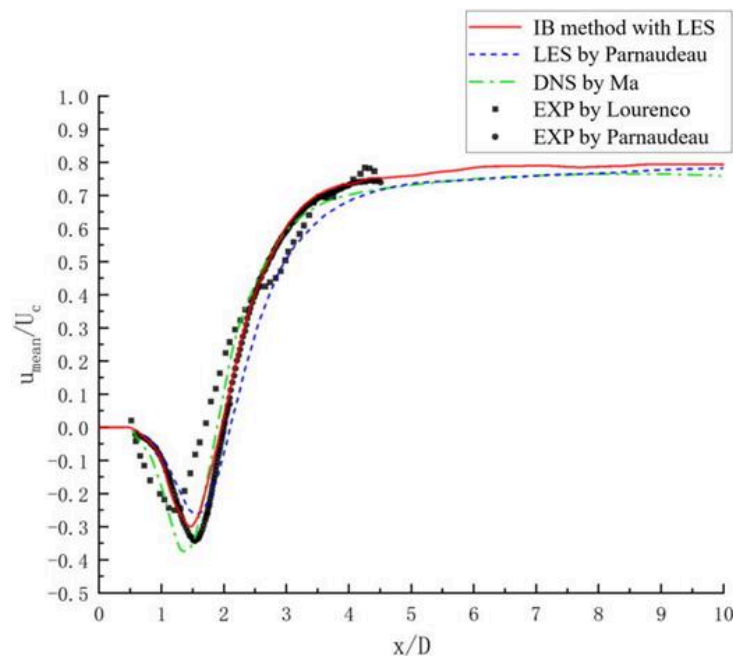
Time-averaged stream-wise relative velocity distribution at the central line.

[Figure 12](#) contrasts the time-averaged streamwise and transverse relative velocities at x/D = 1.06, 1.54, and 2.02 in the central section of the z axis using the IB method with LES, against Parnaudeau's simulation and experimental results. At x/D = 1.06, the IB method shows slight discrepancies, while at x/D = 1.54 and 2.02, the simulation aligns closely with Parnaudeau's data. This performance underscores the IB method's aptitude for accurately simulating the time-averaged variables in the flow field.

FIG. 12.
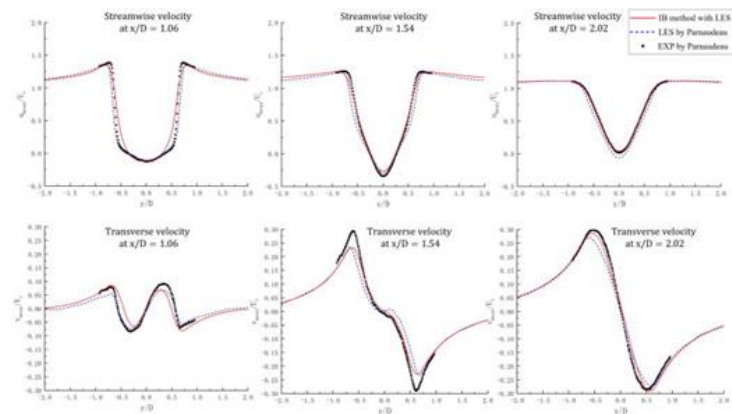
Comparison of time-averaged relative velocities.

In CFD, assessing flow dynamics requires understanding not only the time-averaged velocities, but also the velocity fluctuations. These fluctuations reveal the turbulence intensity and eddy interactions within the flow. The streamwise velocity fluctuation distribution is depicted in **Fig. 13**, while **Fig. 14** illustrates the transverse velocity fluctuation distribution, both of which are key to analyzing the turbulent behavior of the flow around the cylinder.

FIG. 13.
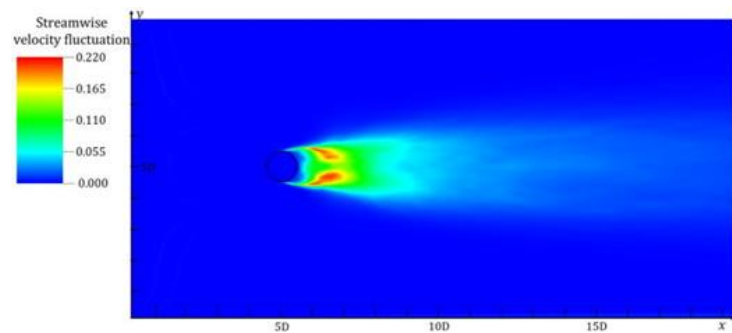
Streamwise velocity fluctuation distribution.

FIG. 14.
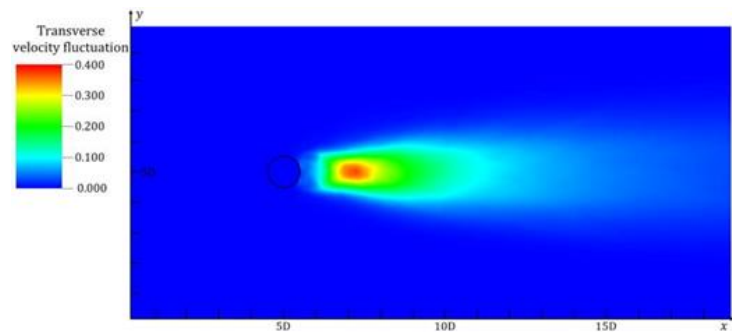
Transverse velocity fluctuation distribution.

Figure 15 provides a detailed comparison of streamwise and transverse velocity fluctuations at sections x/D = 1.06, 1.54, and 2.02, correlating the IB method with LES to literature simulations and experimental data. The IB method effectively captures periodic vortex-induced fluctuations, aligning closely with experimental observations and LES data from Parnaudeau *et al.*, particularly at the downstream locations of x/D = 1.54 and 2.02. This concordance underlines the IB method's proficiency in resolving the intricate turbulent flow near the cylinder with high fidelity.

FIG. 15.
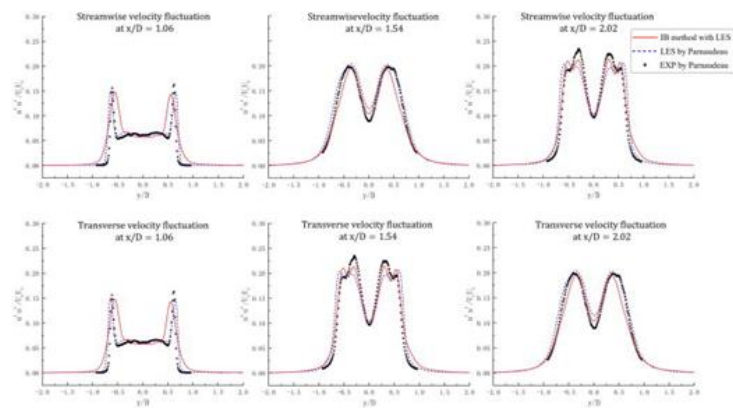
Comparison of velocity fluctuations.

In the analysis of flow around a circular cylinder, parameters such as the average drag coefficient $\overline{C}_d$, the Strouhal number St, the lowest time-averaged streamwise velocity u_{min}/U_c, and the dimensionless average length of the recirculation L_r/D are crucial. **Table I** presents these metrics, derived from the IB method with local reconstruction, together with experimental and literature-based simulation data. This comparison substantiates the reliability of the simulation in estimating the drag coefficient, vortex shedding frequency, minimum velocity, and length of the recirculation zone.

TABLE I.

Comparison of key parameters.

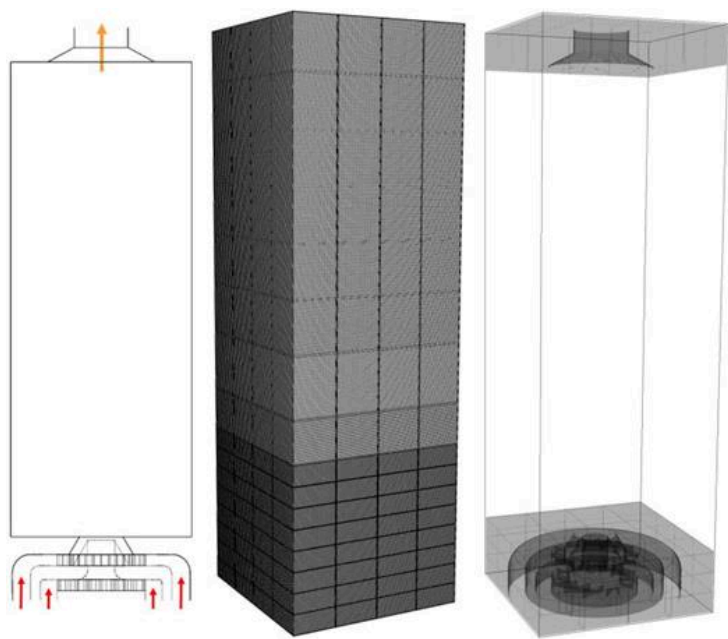| Data source	$\overline{C_d}$	St	u_{min}/U_c	L_r/D
IB method	0.9646	0.2344	−0.2614	1.44
EXP by Lourenco[61]	0.99	0.22	−0.247	1.18
EXP by Ong and Wallace[62]	0.99	0.21	...	1.33
LES by Kravchenko and Moin[63]	1.04	0.21	−0.37	1.35
LES by Parnaudeau et al.[59]	...	0.208	−0.26	1.56
LES by Beaudan[64]	0.92	0.209	...	1.74
LES by Franke and Frank[65]	0.978	0.209	...	1.64

B. Simulation of GTMC

Swirling flames are widely used because of their good ignition performance and stability, as well as the high efficiency of energy conversion in a very limited and small volume, while real combustors are large in size and complex in structure, which are difficult to be measured experimentally in detail. Therefore, a laboratory-scale standard combustor is usually used as the research object instead of the real combustor to perform the validation and optimization of numerical methods. The swirler can create a central recirculation zone that entrains high-temperature gas to stabilize combustion and provide an appropriate amount of air to the reaction zone of the combustor. The design of the swirler structure has a significant impact on the aerodynamic thermal performance of the combustor.

Gas turbine model combustor (GTMC) is a combustor with dual-stage swirler designed by Meier *et al.*,[1,2] based on the grid independence test study previously conducted for the GTMC, the mesh size in this case study is selected to be no larger than 0.5 mm.[39] It was observed that further refinement below this threshold resulted in negligible changes to the velocity distributions obtained from the simulations, indicating that a mesh scale of 0.5 mm is sufficient to capture the essential flow dynamics for this particular configuration. The flow field of the GTMC is simulated using the mesh with 3.49×10^6 grids as shown in **Fig. 16** to check the accuracy of the method in solving the turbulent flow in the twin-swirl combustor. Air flows into the combustor

from the two inlets on the left side of the mesh in a ratio of 1:1.65. The mass flow rate for air is 82 g/s. The inlet temperature is 295 K, and the inlet pressure is 0.4 MPa.
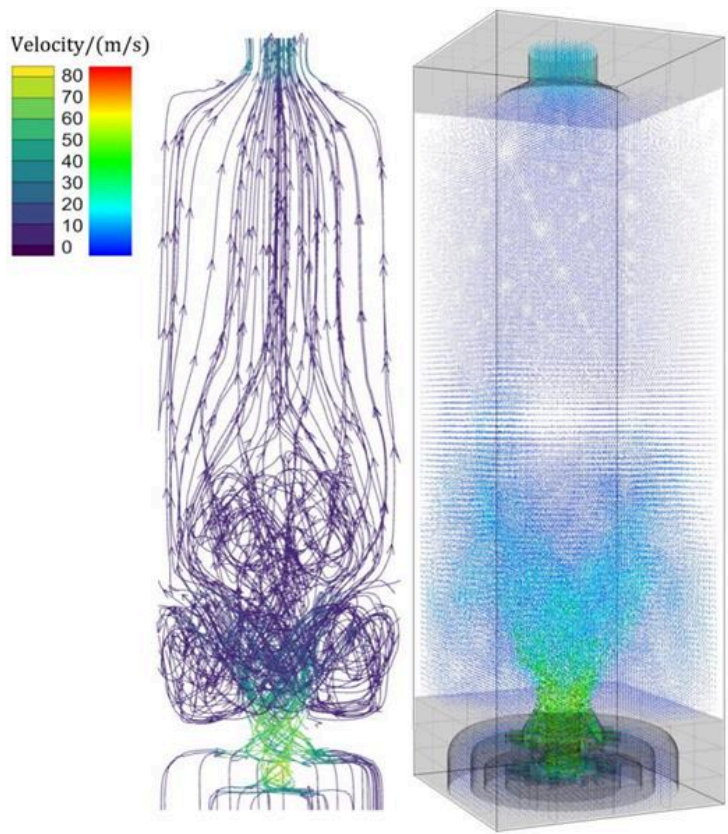
FIG. 16.

Mesh and labels for the GTMC.

Figure 17 shows the velocity vector and 3D streamline of the transient simulation results for the cold flow condition in the negative direction of the x axis.

FIG. 17.

Streamline and transient velocity vector diagram of the GTMC.

The streamline diagram reflects the transient flow situation inside the combustor. There are two recirculation zones behind the swirler. One is the inner recirculation zone (IRZ) formed by vortex breakdown and the other

is the outer recirculation zone (ORZ) formed at the corner near the wall of the combustor.

The IB method in this paper combined with the LES and TPDF methods was written as the aero-engine combustor simulation code based on IB method, and the time-averaged axial velocity simulation result obtained from this method is compared with the simulation result of body-fitted mesh algorithm. The size and shape of the recirculation zones obtained from **Fig. 18**.

FIG. 18.
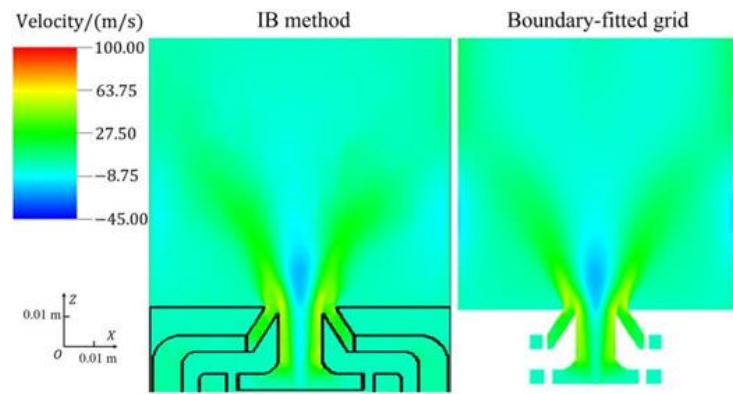
Time-averaged axial velocity diagram at the center interface.

Figure 19 shows the comparison results of the time-averaged axial velocity distribution, the radial velocity distribution, and the tangential velocity distribution behind the swirler outlet of the GTMC, respectively. The objects of comparison are the velocity distribution obtained from this method, the simulation results of body-fitted structured mesh, and the experimental data. The comparison results show that the simulation results of both software are close to the experimental data. Two pairs of axial velocity peaks exist at the closest swirler outlet location (2 mm in height), formed by the inner and outer swirler, respectively. Based on the experimental data, it can be seen that the peaks of the pair close to the axis are relatively higher, that is, relatively high peaks away from the axis in body-fitted mesh simulation results, while the two peaks simulated by this method are more consistent with the experimental data, indicating that this method can simulate the flow field near the dual-stage swirler outlet with greater precision.

FIG. 19.
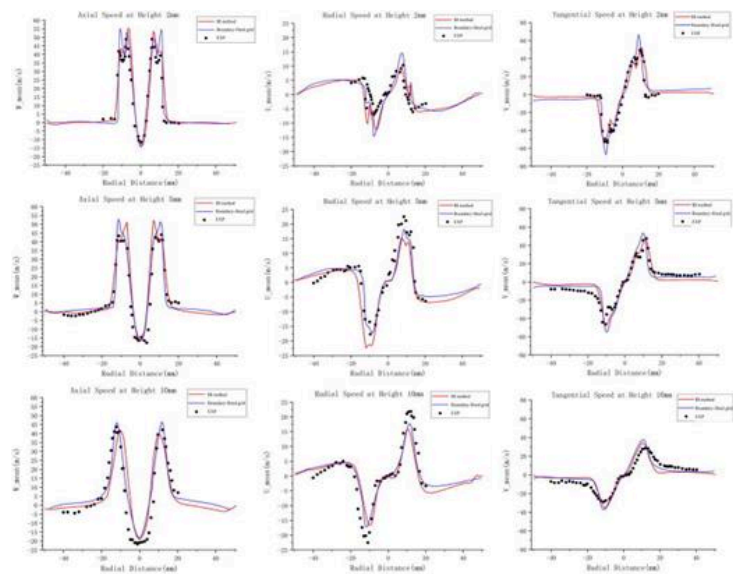
The comparison result of time-averaged velocity distribution.

The average relative errors of the time-averaged velocity distributions in sections at three heights from the swirler outlet are statistically presented in **Table II**. From the table, the average errors of the axial, radial, and tangential velocities averaged in time of the simulation results are 15.7%, 23.8%, and 15.0%. The

corresponding average errors of three velocities from the simulation results of the body-fitted mesh are 14.1%, 18.9%, and 12.2%. The error of the flow field simulation is slightly lower than that of the method due to the higher accuracy near the boundary when solving with a body-fitted structural grid. However, this method has the advantage of reducing the mesh generation workload drastically and generating high-quality mesh quickly. In addition, the overall error of the IB method is close to that of the body-fitted mesh, indicating that it can accurately solve the flow field in the GTMC.

TABLE II.

Relative error of GTMC time-averaged speed.

Height (mm)	Direction	IB method	Body-fitted mesh
2	Axial	13.8%	15.1%
5	Axial	12.0%	11.4%
10	Axial	21.2%	15.8%
2	Radial	36.6%	34.5%
5	Radial	16.9%	11.9%
10	Radial	18.0%	10.2%
2	Tangential	15.4%	11.2%
5	Tangential	11.6%	11.2%
10	Tangential	18.0%	14.3%

## C. Simulation of an aero-engine combustor

The complexity of real aero-engine combustor structures, replete with numerous small-scale features, challenges the application of body-fitted structured meshes in simulations. To address this, the IB method's background mesh labeling significantly eases the creation of high-quality meshes, enhancing the efficiency of parallel combustor simulations. This study examines an annular combustor with 18 identical swirlers, focusing specifically on simulating two-phase turbulent combustion in a segment equivalent to 1/18th of the structure, as depicted in **Fig. 20**. The geometric model of the combustor is discretized into STL format, as illustrated in **Fig. 21**.

FIG. 20.
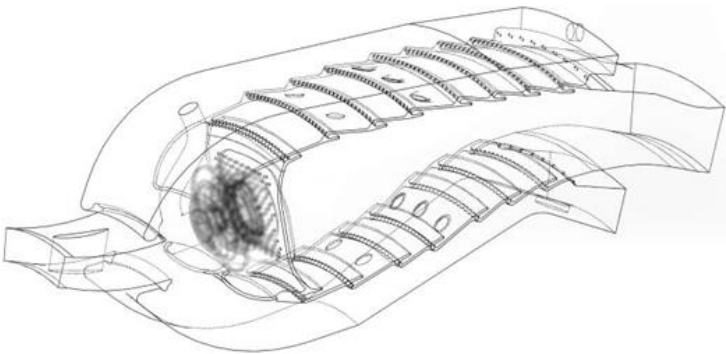
Geometry of the combustor.

FIG. 21.
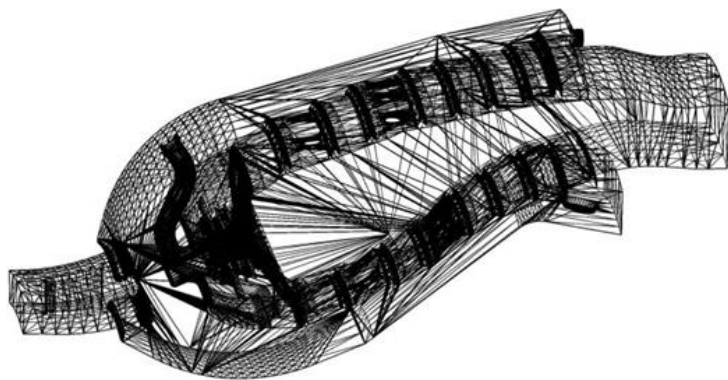
STL of the combustor.

Gas turbine combustors, typically thin-walled and irregularly shaped, require efficient computational domain meshing. As depicted in **Fig. 22**, leveraging a curvilinear coordinate system, the mesh is designed to align with the combustor's geometry. This approach maximizes the inclusion of active fluid computation domains within the grid, minimizing inactive meshes outside the combustion chamber. Consequently, computational resources are conserved, affirming the suitability of this IB method for simulating internal flows in complex thin-walled structures. In the simulation of the aero-engine combustor, a structure and operational analogue to the GTMC but devoid of internal velocity field data, it was observed that refining the mesh size below 0.5 mm yields no significant changes in the distribution of cold-state velocity and pressure. This insight was derived from comparative flow field analyses conducted with 46.37 and 150×10^6 mesh points. Therefore, to ensure the fidelity and efficiency of the simulation while capturing the essential dynamics of the combustor's complex geometry, a mesh size not exceeding 0.5 mm was meticulously chosen across the entire domain, resulting in a total grid count of 46.37×10^6. This approach aligns with the grid independence criterion, affirming the mesh configuration's adequacy for comprehensive combustor simulations. These grids are equally divided into 512 blocks for efficient parallel computation; the computational resource consumption in the simulation is shown in **Table III**.

FIG. 22.
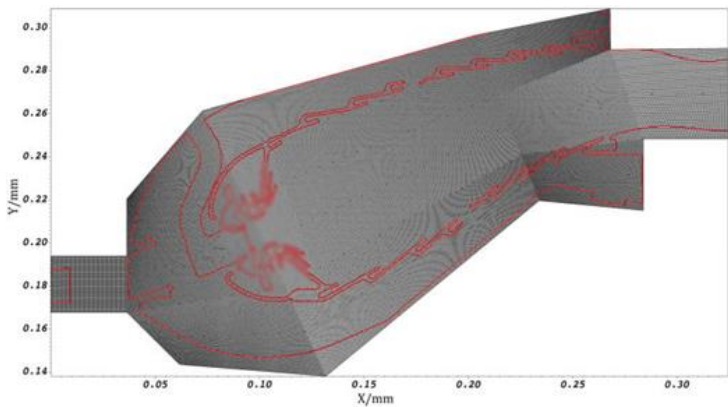
Central section of the mesh.

TABLE III.

Computational resource consumption in aero-engine combustor simulation.

| Project	Parameters
Total number of grids	46.37×10^6
Number of parallel blocks	512
Processor model	AMD EPYC 7452
Number of processors	8

CFL number	0.30
Averaged Δt	3.878×10^{-7} s
Time spent per 1000 steps	2.8 h
Total time steps	160 000

In the simulation of a real combustor, the pressure, temperature, and density of the air compressed by compressor are 790 216.58 Pa, 696.01 K, and 3.955 $\mathrm{kg/m^3}$. The air flows into the diffuser in the positive direction of the x axis at a speed of 121.07 m/s. Fuel at a temperature of 400 K is injected in a conical shape through a nozzle with a radius of 3 mm at a flow rate of 0.0077 kg/s and a Sauter mean diameter value of 39.5 μm in the direction of an angle of 60° with the swirler axis. $\mathrm{C_{12}H_{23}}$ is used as the replacement component for aviation kerosene RP3 and a four-step mechanism[66] is used to simulate the combustion reaction. The fully developed turbulent combustion field is obtained after ignition and a period of time for computation. **Figure 23** (Multimedia available online) shows the 3D streamline of the central cross section in the computed flow field, respectively.

FIG. 23.
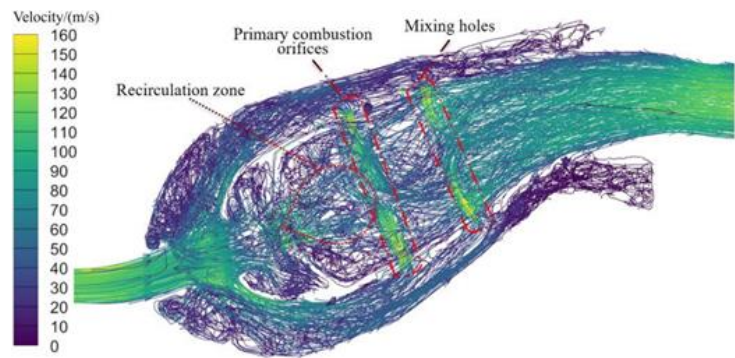
3D streamline diagram. Multimedia available online.
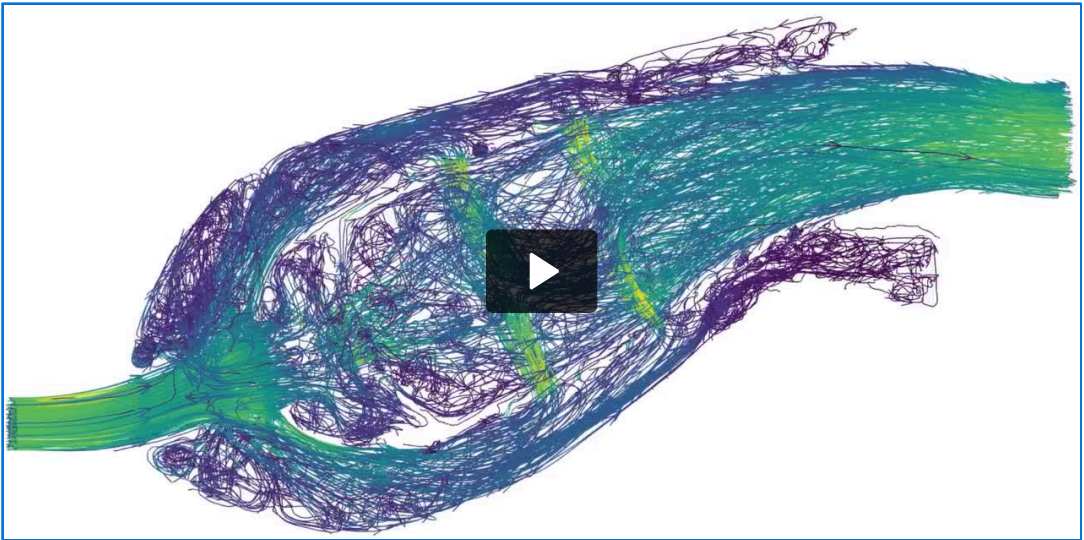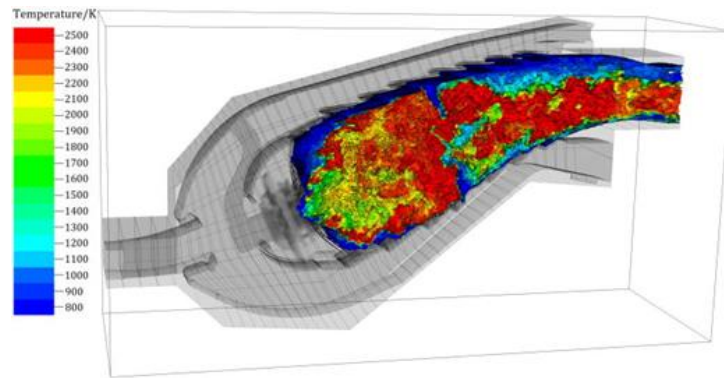

[Video/Audio] available online

In the streamline diagram, the gas flow mainly enters the combustion chamber through the swirler, the main combustion holes, and the dilution holes. The high-speed swirling flow forms a low pressure recirculation zone at the chamber dome shown in **Fig. 24**. An oblique-cut radial dual-stage swirler is used in the combustor. The first-stage oblique cut-hole swirler is mainly used for aerodynamic atomization, and the recirculation zone in **Fig. 24** is mainly formed by the airflow flowing through the second-stage radial swirler.

FIG. 24.
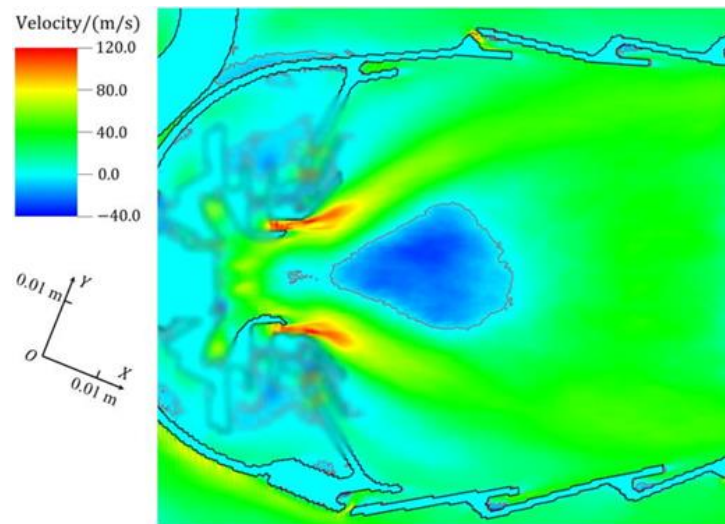
Axial average velocity and recirculation zone of the swirler.

Figure 25 (Multimedia available online) shows the 3D transient temperature field in the central section of the combustor. Fuel droplets behind the nozzle evaporate and absorb heat, creating a low-temperature zone. **Figure 26** shows the mass fraction distribution of the gas-phase evaporated fuel. The gas-phase kerosene undergoes combustion reaction and release intense heat in the front of chamber, which forms a high-temperature zone. There are a large number of waisted step gas film holes on the chamber wall, and the low-temperature air entering from the gas film holes cools the chamber wall to prevent it from overheating.

FIG. 25.

Transient temperature distribution in the central section. Multimedia available online.
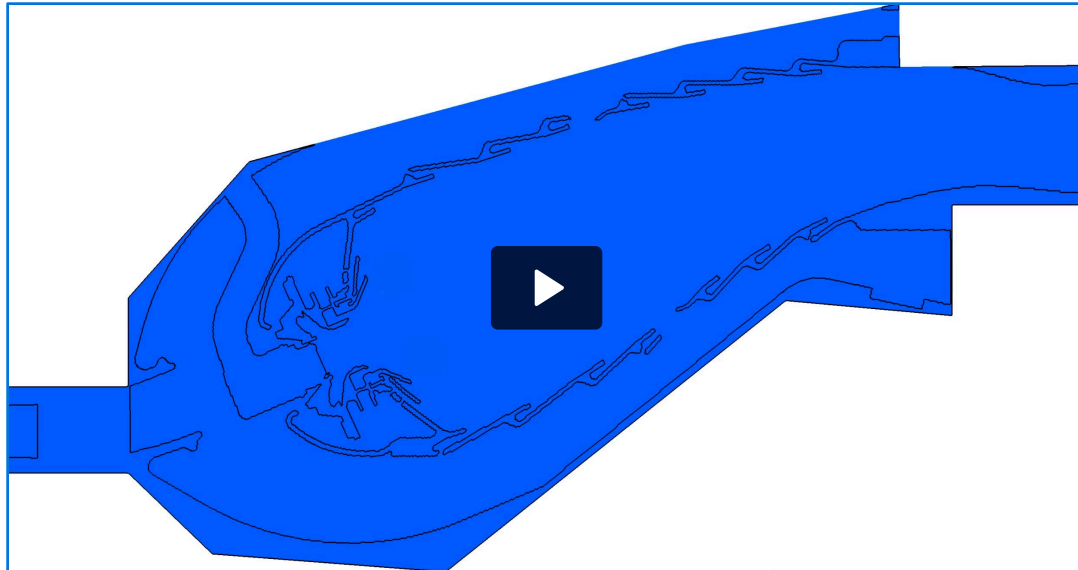
[Video/Audio] available online

FIG. 26.
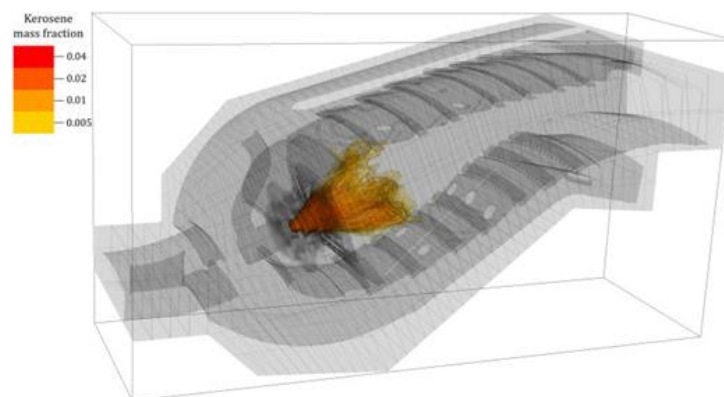
Kerosene distribution in the central section.

The film holes in aero-engine main combustor are small in size, numerous in number, and the function of them is important, but the simulation of them is difficult. Wang *et al.*[67] used the source term method to simulate the airflow through the gas film holes. This method can directly mark the grid of gas film holes, cooling holes, and dilution holes, and can dynamically solve the airflow flux of small holes in combustor simulation.

Figure 27 shows the 3D time average temperature distribution in the central section of the combustor. **Figure 28** shows the shape of the high-temperature zone in the combustion field on a time-average. The high-temperature zone formed by the reaction and heat release of aviation kerosene in the front of the chamber is

cooled by air entering through cooling holes and dilution holes, gradually narrowing along the flow direction, indicating the dilution effect of the cooling airflow.

FIG. 27.
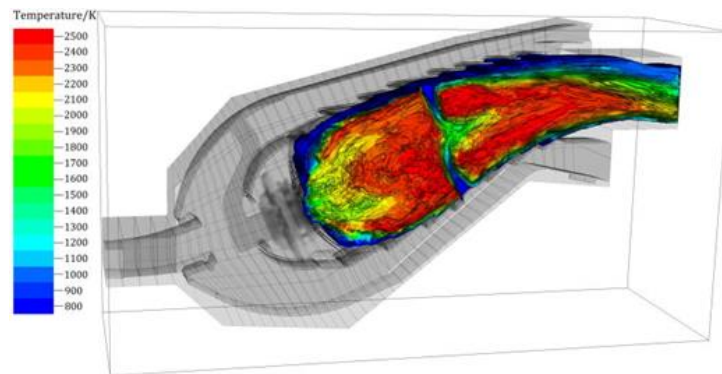
Time-averaged temperature distribution of the central section.

FIG. 28.
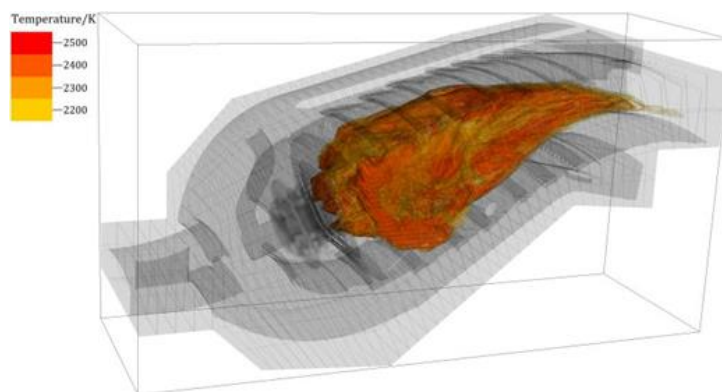
Time-averaged high temperature zone distribution.

By circumferential averaging the time-averaged temperature field in the measuring point cross section at the tail of the chamber, the curve of radial temperature variation with relative height in the measuring point cross section at the tail of the combust chamber is obtained, as shown in **Fig. 29**. The simulated radial temperature distribution at the tail of the chamber is similar to the experimental data.

FIG. 29.
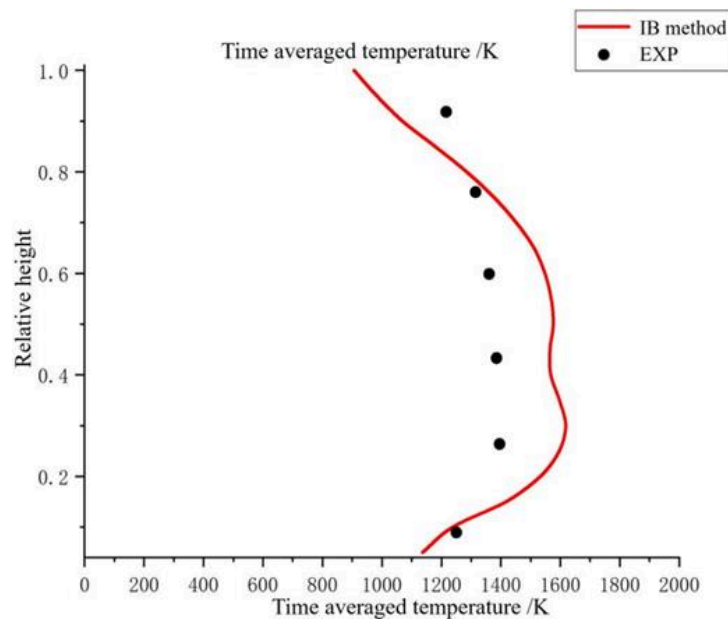
Radial temperature distribution of the measuring points at the exit of the combustor.

In the simulation of the aero-engine combustor, the predominant factors contributing to the observed deviations are identified as the droplet breakup and evaporation models, the chemical reaction mechanisms for aviation kerosene combustion, and the models for turbulent combustion. Distinguished from the simulations that utilize body-fitted structured grids, our IB method demonstrates the capacity to accurately model the intricate structures of real aero-engine combustors. The outcomes yield an exit temperature distribution with errors that are within acceptable limits for engineering applications. Specifically, the maximum relative error in the radial time-averaged temperature distribution across the evaluated cross-section is recorded at 14.8%, with a root mean square error (RMSE) of 11.7%. These results underscore the algorithm's proficiency in replicating the two-phase turbulent combustion process within a genuine combustor configuration, validating its utility for engineering analyses and its superiority in managing complex geometrical challenges.

IV. CONCLUSIONS

The article presents an improved IB method integrated with a geometric scanning algorithm for simulating turbulent flow and combustion in complex geometries, which traverses and reconstructs control volumes at each fluid domain boundary grid point, and indirectly supplements the key information corresponding to the real wall surface obtained by the geometric scanning algorithm to the set of control equations in discrete form through reconstruction.

The improved IB method, integrated with the LES-TPDF model, was applied to simulate various combustion flows. The simulations replicated time-averaged flow fields and pulsation characteristics around a cylinder, mirroring literature data. For the GTMC, simulated velocity and reflux shapes were consistent with boundary-fitted grid algorithms. Deviations from experimental data were minimal for axial, radial, and tangential velocities. The geometric scanning algorithm streamlined grid labeling for complex geometries, enabling resource-efficient, large-scale simulations. This was evidenced by the simulation of an aero-engine combustor that yielded a radial temperature distribution with an RMSE of 11.7%, meeting engineering standards.

The study demonstrates the efficacy of the IB method in providing accurate boundary conditions for combustor simulations, crucially dependent on the match between the provided boundary conditions and the actual physical boundaries. Enhanced by a geometric scanning algorithm, the method efficiently distinguishes between fluid and solid domains and incorporates detailed information such as real boundary locations and normal vectors for precise local reconstruction. This approach ensures the suitability of the IB method for realistic gas turbine combustor simulations, offering valuable insights for advanced engineering design.

ACKNOWLEDGMENTS

AUTHOR DECLARATIONS

Conflict of Interest

The authors have no conflicts to disclose.

Author Contributions

Yudong Wang: Conceptualization (equal); Data curation (equal); Formal analysis (equal); Investigation (equal); Methodology (equal); Software (equal); Validation (equal); Writing—original draft (equal). **Fang Wang:** Conceptualization (equal); Data curation (equal); Funding acquisition (equal); Methodology (equal); Project administration (equal); Resources (equal); Software (equal); Supervision (equal); Writing—review & editing (equal). **Jiawei Zhou:** Data curation (equal); Formal analysis (equal); Methodology (supporting); Project administration (supporting); Software (equal); Validation (equal); Visualization (equal). **Jie Jin:** Conceptualization (equal); Funding acquisition (equal); Investigation (equal); Methodology (equal); Project administration (equal); Resources (equal); Supervision (equal).

DATA AVAILABILITY

The data that support the findings of this study are available from the corresponding author upon reasonable request.

REFERENCES

1. U. Meier , J. Heinze , S. Freitag , and C. Hassa , " Spray and flame structure of a generic injector at aeroengine conditions," in Proceedings of the ASME 2011 Turbo Expo: Power for Land, Sea, and Air (American Society of Mechanical Engineers, 2011), pp. 61–72.
Google Scholar　　Crossref

2. S. Freitag , U. Meier , J. Heinze , T. Behrendt , and C. Hassa , " Measurement of initial conditions of a kerosene spray from a generic aeroengine injector at elevated pressure," *Atomization Sprays* 21, 521 (2011). https://doi.org/10.1615/AtomizSpr.2011003457
Google Scholar　　Crossref

3. R. Mittal and G. Iaccarino , " Immersed boundary methods," *Annu. Rev. Fluid Mech.* 37, 239 (2005). https://doi.org/10.1146/annurev.fluid.37.061903.175743
Google Scholar　　Crossref

4. R. Verzicco , " Immersed boundary methods: Historical perspective and future outlook," *Annu. Rev. Fluid Mech.* 55, 129 (2023). https://doi.org/10.1146/annurev-fluid-120720-022129
Google Scholar　　Crossref

5. C. S. Peskin , " Flow patterns around heart valves: A numerical method," *J. Comput. Phys.* 10, 252 (1972). https://doi.org/10.1016/0021-9991(72)90065-4
Google Scholar　　Crossref

6. S. K. Kang and Y. A. Hassan , " A comparative study of direct-forcing immersed boundary-lattice Boltzmann methods for stationary complex boundaries," *Int. J. Numer. Methods Fluids* 66, 1132 (2011). https://doi.org/10.1002/fld.2304
Google Scholar　　Crossref

7. C. Liu and C. Hu , " An efficient immersed boundary treatment for complex moving object," *J. Comput. Phys.* 274, 654 (2014). https://doi.org/10.1016/j.jcp.2014.06.042
Google Scholar　　Crossref

8. M. Kumar , S. Roy , and M. S. Ali , " An efficient immersed boundary algorithm for simulation of flows in curved and moving geometries," *Comput. Fluids* 129, 159 (2016). https://doi.org/10.1016/j.compfluid.2016.02.009
Google Scholar　　Crossref

9. J. R. Nezhad and S. A. Mirbozorgi , " An immersed boundary-lattice Boltzmann method to simulate chaotic micromixers with baffles," *Comput. Fluids* 167, 206 (2018). https://doi.org/10.1016/j.compfluid.2018.02.031
Google Scholar   Crossref

10. X. Wang , X. Gong , K. Sugiyama , S. Takagi , and H. Huang , " An immersed boundary method for mass transfer through porous biomembranes under large deformations," *J. Comput. Phys.* 413, 109444 (2020). https://doi.org/10.1016/j.jcp.2020.109444
Google Scholar   Crossref

11. X. Sun and M. Sakai , " Numerical simulation of two-phase flows in complex geometries by using the volume-of-fluid/immersed-boundary method," *Chem. Eng. Sci.* 139, 221 (2016). https://doi.org/10.1016/j.ces.2015.09.031
Google Scholar   Crossref

12. B. Blais , M. Lassaigne , C. Goniva , L. Fradette , and F. Bertrand , " A semi-implicit immersed boundary method and its application to viscous mixing," *Comput. Chem. Eng.* 85, 136 (2016). https://doi.org/10.1016/j.compchemeng.2015.10.019
Google Scholar   Crossref

13. L. Wang , G. M. Currao , F. Han , A. J. Neely , J. Young , and F.-B. Tian , " An immersed boundary method for fluid–structure interaction with compressible multiphase flows," *J. Comput. Phys.* 346, 131 (2017). https://doi.org/10.1016/j.jcp.2017.06.008
Google Scholar   Crossref

14. B. Vadala-Roth , S. Acharya , N. A. Patankar , S. Rossi , and B. E. Griffith , " Stabilization approaches for the hyperelastic immersed boundary method for problems of large-deformation incompressible elasticity," *Comput. Methods Appl. Mech. Eng.* 365, 112978 (2020). https://doi.org/10.1016/j.cma.2020.112978
Google Scholar   Crossref   PubMed

15. Y. Zhang , G. Pan , Y. Zhang , and S. Haeri , " A relaxed multi-direct-forcing immersed boundary-cascaded lattice Boltzmann method accelerated on GPU," *Comput. Phys. Commun.* 248, 106980 (2020). https://doi.org/10.1016/j.cpc.2019.106980
Google Scholar   Crossref

16. B. E. Griffith and N. A. Patankar , " Immersed Methods for Fluid–Structure Interaction," *Annu. Rev. Fluid Mech.* 52, 421 (2020). https://doi.org/10.1146/annurev-fluid-010719-060228
Google Scholar   Crossref   PubMed

17. J. Mohd-Yusof , " Development of immersed boundary methods for complex geometries," *Annu. Res. Briefs* 1998, 325.

18. R. P. Fedkiw , T. Aslam , B. Merriman , and S. Osher , " A non-oscillatory Eulerian approach to interfaces in multimaterial flows (the ghost fluid method)," *J. Comput. Phys.* 152, 457 (1999). https://doi.org/10.1006/jcph.1999.6236
Google Scholar   Crossref

19. A. Gilmanov , F. Sotiropoulos , and E. Balaras , " A general reconstruction algorithm for simulating flows with complex 3D immersed boundaries on Cartesian grids," *J. Comput. Phys.* 191, 660 (2003). https://doi.org/10.1016/S0021-9991(03)00321-8
Google Scholar   Crossref

20. H. Kor , M. B. Ghomizad , and K. Fukagata , " A unified interpolation stencil for ghost-cell immersed boundary method for flow around complex geometries," *J. Fluid Sci. Technol.* 12, JFST0011 (2017). https://doi.org/10.1299/jfst.2017jfst0011
Google Scholar   Crossref

21. J. Nam and F. Lien , " A ghost-cell immersed boundary method for large-eddy simulations of compressible turbulent flows," *Int. J. Comput. Fluid Dyn.* 28, 41 (2014). https://doi.org/10.1080/10618562.2014.887072
Google Scholar   Crossref

22. T. Ye , R. Mittal , H. Udaykumar , and W. Shyy , " An accurate Cartesian grid method for viscous incompressible flows with complex immersed boundaries," *J. Comput. Phys.* 156, 209 (1999). https://doi.org/10.1006/jcph.1999.6356
Google Scholar   Crossref

23.   S. Majumdar , G. Iaccarino , P. Durbin et al, " RANS solvers with adaptive structured boundary non-conforming grids," *Annu. Res. Briefs* 1, 179 (2001).
Google Scholar

24.   H. Udaykumar , R. Mittal , P. Rampunggoon , and A. Khanna , " A sharp interface Cartesian grid method for simulating flows with complex moving boundaries," *J. Comput. Phys.* 174, 345 (2001). https://doi.org/10.1006/jcph.2001.6916
Google Scholar   Crossref

25.   J.-D. Lee , *Development of an Efficient Viscous Approach in a Cartesian Grid Framework and Application to Rotor-Fuselage Interaction* (Georgia Institute of Technology, 2006).
Google Scholar

26.   S. Tan and C.-W. Shu , " Inverse Lax–Wendroff procedure for numerical boundary conditions of conservation laws," *J. Comput. Phys.* 229, 8144 (2010). https://doi.org/10.1016/j.jcp.2010.07.014
Google Scholar   Crossref

27.   S. Tan , C. Wang , C.-W. Shu , and J. Ning , " Efficient implementation of high order inverse Lax–Wendroff boundary treatment for conservation laws," *J. Comput. Phys.* 231, 2510 (2012). https://doi.org/10.1016/j.jcp.2011.11.037
Google Scholar   Crossref

28.   L. Huang , C.-W. Shu , and M. Zhang , " Numerical boundary conditions for the fast sweeping high order WENO methods for solving the Eikonal equation," *J. Comput. Math.* 26, 336 (2008).
Google Scholar

29.   T. Xiong , M. Zhang , Y.-T. Zhang , and C.-W. Shu , " Fast sweeping fifth order WENO scheme for static Hamilton–Jacobi equations with accurate boundary treatment," *J. Sci. Comput.* 45, 514 (2010). https://doi.org/10.1007/s10915-010-9345-6
Google Scholar   Crossref

30.   S. Clain , D. Lopes , and R. M. Pereira , " Very high-order Cartesian-grid finite difference method on arbitrary geometries," *J. Comput. Phys.* 434, 110217 (2021). https://doi.org/10.1016/j.jcp.2021.110217
Google Scholar   Crossref

31.   D. Appelo and N. A. Petersson , " A fourth-order accurate embedded boundary method for the wave equation," *SIAM J. Sci. Comput.* 34, A2982 (2012). https://doi.org/10.1137/09077223X
Google Scholar   Crossref

32.   R. Meakin and R. Meakin , " On adaptive refinement and overset structured grids," AIAA Paper No. 97-1858, 1997.
Google Scholar

33.   A. M. Roma , C. S. Peskin , and M. J. Berger , " An adaptive version of the immersed boundary method," *J. Comput. Phys.* 153, 509 (1999). https://doi.org/10.1006/jcph.1999.6293
Google Scholar   Crossref

34.   S. M. Ruffin , M. Zaki , and S. Sekhar , " A normal ray refinement technique for Cartesian-grid based Navier–Stokes solvers," *Int. J. Comput. Fluid Dyn.* 26, 231 (2012). https://doi.org/10.1080/10618562.2012.691970
Google Scholar   Crossref

35.   K. Anupindi , Y. Delorme , D. A. Shetty , and S. H. Frankel , " A novel multiblock immersed boundary method for large eddy simulation of complex arterial hemodynamics," *J. Comput. Phys.* 254, 200 (2013). https://doi.org/10.1016/j.jcp.2013.07.033
Google Scholar   Crossref

36.   Y. T. Delorme , M. D. Rodefeld , and S. H. Frankel , " Multiblock high order large eddy simulation of powered Fontan hemodynamics: Towards computational surgery," *Comput. Fluids* 143, 16 (2017). https://doi.org/10.1016/j.compfluid.2016.10.032
Google Scholar   Crossref   PubMed

37.   D. de Zelicourt , L. Ge , C. Wang , F. Sotiropoulos , A. Gilmanov , and A. Yoganathan , " Flow simulations in arbitrarily complex cardiovascular anatomies—An unstructured Cartesian grid approach," *Comput. Fluids* 38, 1749 (2009). https://doi.org/10.1016/j.compfluid.2009.03.005
Google Scholar   Crossref

38.   C. Zhu , J.-H. Seo , and R. Mittal , " A graph-partitioned sharp-interface immersed boundary solver for efficient solution of internal flows," *J. Comput. Phys.* 386, 37 (2019).

https://doi.org/10.1016/j.jcp.2019.01.038

Google Scholar   Crossref

39.   W. Jones , A. Marquis , and K. Vogiatzaki , " Large-eddy simulation of spray combustion in a gas turbine combustor," *Combust. Flame* 161, 222 (2014). https://doi.org/10.1016/j.combustflame.2013.07.016

Google Scholar   Crossref

40.   Z. Yu , J-l Le , and Y. HUANG , " LES of combustion flow field in a practical aeroengine combustor with two-stage counter-rotating swirler," *J. Propul. Technol.* 39, 1576 (2018).

Google Scholar

41.   A. M. Roma , *A Multilevel Self Adaptive Version of the Immersed Boundary Method* (New York University, 1996).

Google Scholar

42.   U. Piomelli and E. Balaras , " Wall-layer models for large -eddy simulations," *Annu. Rev. Fluid Mech.* 34, 349 (2002). https://doi.org/10.1146/annurev.fluid.34.082901.144919

Google Scholar   Crossref

43.   W. Fang , L. Rui , D. Li , L. Denghuan , and J. Jie , " A dual timescale model for micro-mixing and its application in LES-TPDF simulations of turbulent nonpremixed flames," *Chin. J. Aeronaut.* 32, 875 (2019). https://doi.org/10.1016/J.CJA.2019.01.005

Google Scholar   Crossref

44.   F. Wang , Y. Wang , G. Wei , D. Liu , J. Jin , and W. P. Jones , " Flame structure of methane and kerosene combustion with a compact concave flame-holder using the LES-PDF method," *J. Therm. Sci.* 33, 222 (2023). https://doi.org/10.1007/s11630-023-1898-4

Google Scholar   Crossref

45.   W. Jones and S. Navarro-Martinez , " Numerical study of n-heptane auto-ignition using LES-pdf methods," *Flow, Turbul. Combust.* 83, 407 (2009). https://doi.org/10.1007/s10494-009-9228-9

Google Scholar   Crossref

46.   D. Fredrich , W. P. Jones , and A. J. Marquis , " Thermo-acoustic instabilities in the PRECCINSTA combustor investigated using a compressible LES-pdf approach," *Flow, Turbul. Combust.* 106, 1399 (2021). https://doi.org/10.1007/s10494-020-00177-3

Google Scholar   Crossref

47.   Z. Wu and L. Guo , " Accuracy improvement of immersed boundary-lattice Boltzmann and finite element method by iterative velocity correction," *Phys. Fluids* 34, 103102 (2022). https://doi.org/10.1063/5.0110813

Google Scholar   Crossref

48.   A. Lagae and P. Dutré , " An efficient ray-quadrilateral intersection test," *J. Graph. Tools* 10, 23 (2005). https://doi.org/10.1080/2151237X.2005.10129208

Google Scholar   Crossref

49.   X. Niu , C. Shu , Y. Chew , and Y. Peng , " A momentum exchange-based immersed boundary-lattice Boltzmann method for simulating incompressible viscous flows," *Phys. Lett. A* 354, 173 (2006). https://doi.org/10.1016/j.physleta.2006.01.060

Google Scholar   Crossref

50.   J. M. Stockie and B. T. Wetton , " Stability analysis for the immersed fiber problem," *SIAM J. Appl. Math.* 55, 1577 (1995). https://doi.org/10.1137/S0036139994267018

Google Scholar   Crossref

51.   J. M. Stockie and B. R. Wetton , " Analysis of stiffness in the immersed boundary method and implications for time-stepping schemes," *J. Comput. Phys.* 154, 41 (1999). https://doi.org/10.1006/jcph.1999.6297

Google Scholar   Crossref

52.   F. Gao and E. E. O'Brien , " A large-eddy simulation scheme for turbulent reacting flows," *Phys. Fluids A* 5, 1282 (1993). https://doi.org/10.1063/1.858617

Google Scholar   Crossref

53.   C. Dopazo and E. E. O'Brien , " Functional formulation of nonisothermal turbulent reactive flows," *Phys. Fluids* 17, 1968 (1974). https://doi.org/10.1063/1.1694652

Google Scholar   Crossref

54. W. Jones , A. Marquis , and V. Prasad , " LES of a turbulent premixed swirl burner using the Eulerian stochastic field method," *Combust. Flame* 159, 3079 (2012).
https://doi.org/10.1016/j.combustflame.2012.04.008
Google Scholar   Crossref

55. W. Jones and S. Navarro-Martinez , " Large eddy simulation of autoignition with a subgrid probability density function method," *Combust. Flame* 150, 170 (2007).
https://doi.org/10.1016/j.combustflame.2007.04.003
Google Scholar   Crossref

56. W. Jones and V. Prasad , " Large eddy simulation of the Sandia Flame series (D–F) using the Eulerian stochastic field method," *Combust. Flame* 157, 1621 (2010).
https://doi.org/10.1016/j.combustflame.2010.05.010
Google Scholar   Crossref

57. R. Mustata , L. Valiño , C. Jiménez , W. Jones , and S. Bondi , " A probability density function Eulerian Monte Carlo field method for large eddy simulations: Application to a turbulent piloted methane/air diffusion flame (Sandia D)," *Combust. Flame* 145, 88 (2006).
https://doi.org/10.1016/j.combustflame.2005.12.002
Google Scholar   Crossref

58. S. Sarkar and S. Sarkar , " Simulation of vortex dynamics in a cylinder wake by the Immersed Boundary technique," *Prog. Comput. Fluid Dyn.* 10, 129 (2010).
https://doi.org/10.1504/PCFD.2010.033325
Google Scholar   Crossref

59. P. Parnaudeau , J. Carlier , D. Heitz , and E. Lamballais , " Experimental and numerical studies of the flow over a circular cylinder at Reynolds number 3900," *Phys. Fluids* 20, 085101 (2008).
https://doi.org/10.1063/1.2957018
Google Scholar   Crossref

60. X. Ma , G.-S. Karamanos , and G. Karniadakis , " Dynamics and low-dimensionality of a turbulent near wake," *J. Fluid Mech.* 410, 29 (2000). https://doi.org/10.1017/S0022112099007934
Google Scholar   Crossref

61. L. Lourenco , A particle image velocimetry study (1993).

62. L. Ong and J. Wallace , " The velocity field of the turbulent very near wake of a circular cylinder," *Exp. Fluids* 20, 441 (1996). https://doi.org/10.1007/BF00189383
Google Scholar   Crossref

63. A. G. Kravchenko and P. Moin , " Numerical studies of flow over a circular cylinder at $Re_D = 3900$," *Phys. Fluids* 12, 403 (2000). https://doi.org/10.1063/1.870318
Google Scholar   Crossref

64. P. B. Beaudan , *Numerical Experiments on the Flow past a Circular Cylinder at Sub-Critical Reynolds Number* (Stanford University, 1995).
Google Scholar

65. J. Franke and W. Frank , " Large eddy simulation of the flow past a circular cylinder at $Re_D = 3900$," *J. Wind Eng. Ind. Aerodyn.* 90, 1191 (2002). https://doi.org/10.1016/S0167-6105(02)00232-5
Google Scholar   Crossref

66. K. Kundu and J. Deur , " A simplified reaction mechanism for calculation of emissions in hydrocarbon (Jet-A) combustion," AIAA Paper No. 93-2341, 1993.
Google Scholar

67. J. Wang , R. Mao , W. Tao , Z. Wang , C. Zhang , and Y. Lin , " Numerical simulation of combustor effusion cooling flow based on source term method," in Proceedings of the ASME 2011 Turbo Expo: Power for Land, Sea, and Air (American Society of Mechanical Engineers, 2019), paper no. V05BT17A001.
Google Scholar   Crossref